JOURNAL OF GEOPHYSICAL RESEARCH: OCEANS, VOL. 118, 6461–6478, doi:10.1002/2013JC009228, 2013

Temporal variability of the meridional overturning circulation at 34.5°S: Results from two pilot boundary arrays in the South Atlantic

Christopher S. Meinen,[1] Sabrina Speich,[2] Renellys C. Perez,[1,3] Shenfu Dong,[1,3] Alberto R. Piola,[4] Silvia L. Garzoli,[1,3] Molly O. Baringer,[1] Sergey Gladyshev,[5] and Edmo J. D. Campos[6]

Received 21 June 2013; revised 16 September 2013; accepted 6 November 2013; published 3 December 2013.

[1] Data from two boundary arrays deployed along 34.5°S are combined to produce the first continuous in situ time series observations of the basin-wide meridional overturning circulation (MOC) in the South Atlantic. Daily estimates of the MOC between March 2009 and December 2010 range between 3 Sv and 39 Sv (1 Sv = 10^6 m^3 s^{-1}) after a 10 day low-pass filter is applied. Much of the variability in this ~20 month record occurs at periods shorter than 100 days. Approximately two-thirds of the MOC variability is due to changes in the geostrophic (baroclinic plus barotropic) volume transport, with the remainder associated with the direct wind-forced Ekman transport. When low-pass filtered to match previously published analyses in the North Atlantic, the observed temporal standard deviation at 34.5°S matches or somewhat exceeds that observed by time series observations at 16°N, 26.5°N, and 41°N. For periods shorter than 20 days the basin-wide MOC variations are most strongly influenced by Ekman flows, while at periods between 20 and 90 days the geostrophic flows tend to exert slightly more control over the total transport variability of the MOC. The geostrophic shear variations are roughly equally controlled by density variations on the western and eastern boundaries at all time scales captured in the record. The observed time-mean MOC vertical structure and temporal variability agree well with the limited independent observations available for confirmation.

Citation: Meinen, C. S., S. Speich, R. C. Perez, S. Dong, A. R. Piola, S. L. Garzoli, M. O. Baringer, S. Gladyshev, and E. J. D. Campos (2013), Temporal variability of the meridional overturning circulation at 34.5°S: Results from two pilot boundary arrays in the South Atlantic, *J. Geophys. Res. Oceans*, *118*, 6461–6478, doi:10.1002/2013JC009228.

1. Introduction

[2] Variations in the meridional overturning circulation (MOC) have been shown to be correlated to changes in important climate signals including surface air temperatures, precipitation, and hurricane intensity over much of the northern hemisphere [e.g., *Vellinga and Wood*, 2002; *Stouffer et al*., 2006; *Zhang and Delworth*, 2006]. Continuous basin-wide, full-water-column time series measurements of the MOC have been made for nearly a decade at 26.5°N in the North Atlantic [e.g., *Cunningham et al*., 2007; *Kanzow et al*., 2010; *Johns et al*., 2011], and less complete but longer time series of the MOC have been estimated near 41°N and 16°N [e.g., *Willis and Fu*, 2008; *Send et al*., 2011]. These measurements have revealed a much more variable MOC than had previously been expected, with strong variations at time scales ranging from a few weeks to months [e.g., *Cunningham et al*., 2007] and significant variability on seasonal to interannual timescales [e.g., *Kanzow et al*., 2010; *McCarthy et al*., 2012]. One of the first realizations that has come from the mooring data at 26.5°N is that the significant low-frequency variability that is observed cannot be adequately captured by a limited number of snapshot sections collected across decades, as such analyses will almost inevitably alias higher frequency variations into artificial trends or longer-period variability [e.g., *Bryden et al*., 2005; *Kanzow et al*., 2010].

[3] The successes of the trans-basin array at 26.5°N and the other North Atlantic MOC observing systems have provided many insights, but they have also raised several new questions, such as the degree to which MOC fluctuations are correlated meridionally as well as the mechanisms associated with the complex phasing between atmospheric forcing and intrinsic variability [e.g., *Zhang*, 2010; *Zhang et al*., 2011]. Furthermore during the decade or so when these observations have been collected, a wide range

[1]NOAA/Atlantic Oceanographic and Meteorological Laboratory, Physical Oceanography Division, Miami, Florida, USA.
[2]Laboratoire de Physique des Océans, University of Brest and IFREMER, Brest, France.
[3]Cooperative Institute for Marine and Atmospheric Studies, University of Miami, Miami, Florida, USA.
[4]Servicio de Hidrografía Naval, and Universidad de Buenos Aires, UMI IFAECI/CONICET/CNRS, Buenos Aires, Argentina.
[5]Shirshov Institute of Oceanology, Moscow, Russia.
[6]Oceanographic Institute, University of Sao Paulo, Sao Paulo, Brazil.

Corresponding author: C. S. Meinen, Atlantic Oceanographic and Meteorological Laboratory, Physical Oceanography Division, 4301 Rickenbacker Causeway, Miami, FL 33149, USA. (Christopher.Meinen@noaa.gov)

2169-9275/13/10.1002/2013JC009228

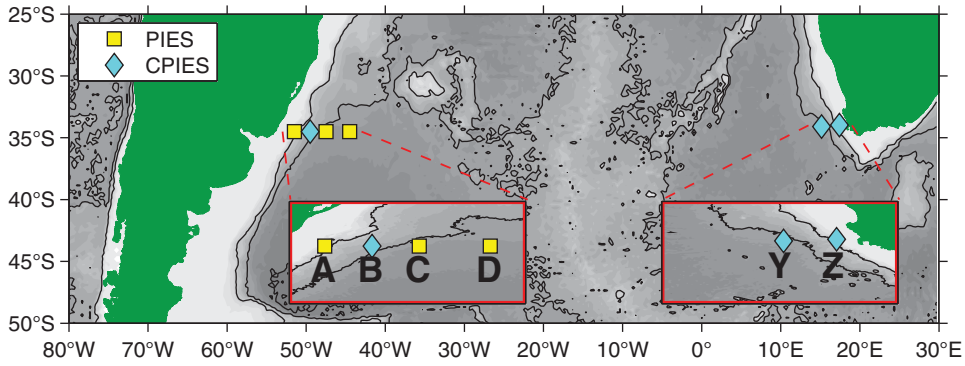

Figure 1. Locations of the two boundary arrays. The names of each site are indicated by bold letters, while the type of instrument is noted in the legend. Bottom topography from *Smith and Sandwell* [1997] is denoted by gray shading with the 2000 and 4000 dbar isobaths highlighted as black contours.

of theoretical and numerical modeling studies have demonstrated that the variability in the subtropical North Atlantic is only one facet of a complex circulation system, with significant variability and forcing introduced in the South Atlantic, for example [e.g., *Garzoli and Matano*, 2011, and references therein]. Expanding the MOC observing system has proven challenging, however key components of the MOC are being measured by time series arrays deployed in a variety of locations including at the Denmark Strait [e.g., *Jochumsen et al*., 2012], at 42°N [e.g., *Toole et al*., 2011; *Peña-Molino et al*., 2012] and at 16°N [e.g., *Kanzow et al*., 2008; *Send et al*., 2011]. Time series measurements have also been obtained across Drake Passage and south of South Africa where inter-ocean exchanges of mass, heat and salt crucial to the global MOC occur [e.g., *Chereskin et al*., 2009]. Furthermore, within the South Atlantic itself, regular trans-basin hydrographic and expendable bathythermograph (XBT) section observations have been collected at selected latitudes such as 24°S [e.g., *Bryden et al*., 2011; *McCarthy et al*., 2011], 30°S [*McDonagh and King*, 2005], and 34.5°S [e.g., *Baringer and Garzoli*, 2007; *Garzoli and Baringer*, 2007; *Dong et al*., 2009; *Garzoli et al*., 2013]. Recent observing system design studies have suggested that, of the South Atlantic latitudes, 34.5°S would be ideal for capturing MOC variability at the "mouth" of the Atlantic basin [*Perez et al*., 2011]. This location is also well supported by theoretical analyses that suggest that crucial MOC stability evaluations would be best applied as far from the equator in the South Atlantic as possible [e.g., *Dijkstra*, 2007; *Drijfhout et al*., 2011].

[4] In the subtropical South Atlantic the character of the MOC is somewhat different than at 26.5°N in the North Atlantic in that at 34.5°S the northward flowing warm upper limb of the MOC is primarily found near to the eastern boundary in the Benguela Current and Agulhas Rings, while in the North Atlantic at 26.5°N the upper limb of the MOC is primarily found near to the western boundary. As such, it is more critical in the South Atlantic to have detailed, well resolved measurements near both boundaries. Pilot arrays designed to measure the density structure and the flows at the eastern and western boundaries of the basin along 34.5°S (Figure 1) were deployed in February 2008 and March 2009, respectively [e.g., *Speich and Dehairs*, 2008; *Meinen et al*., 2012]. The western array, known as the Southwest Atlantic MOC array, has been making measurements continuously from March 2009 to the present; the eastern array, deployed as part of the GoodHope program, was in place from February 2008 to December 2010. The two arrays overlapped in time for approximately 20 months from 20 March 2009 to 2 December 2010. These records, when analyzed together with wind and other observations, provide the first opportunity to estimate the daily time series of basin-wide MOC transport at 34.5°S using in situ observations. This article presents an initial analysis of the variability of the MOC at 34.5°S using data collected by these pilot arrays. The results are compared to concurrent snapshot estimates from basin-wide XBT sections as well as estimates from other in situ data and numerical model products.

2. Data

[5] Inverted echo sounders (IES) have been in use for many years in a variety of regions [e.g., *Rossby*, 1969; *Watts and Rossby*, 1977] including the western and eastern boundaries of the South Atlantic [*Garzoli*, 1993; *Garzoli and Gordon*, 1996]. The IES can be equipped with additional sensors including a pressure sensor (called a "PIES") as well as a single depth current meter and pressure sensor (called a "CPIES"); both have been in routine use over the past few decades [e.g., *Watts et al*., 1995; *Meinen*, 2001; *Chereskin et al*., 2009; *Donohue et al*., 2010]. The present day techniques involved in analyzing inverted echo sounder data are well established [e.g., *Meinen and Watts*, 2000; *Watts et al*., 2001], and will be reviewed here only inasmuch as they illustrate specifics associated with the application in these regions and relate to the analysis of the two arrays of PIES/CPIES discussed in this study (Figure 1) [see also *Speich and Dehairs*, 2008; *Meinen et al*., 2012].

[6] The western array, which has collected about 4 years of data to date, initially consisted of one CPIES and three PIES (the CPIES has subsequently been replaced with a PIES). The eastern array, which was recovered in December 2010, consisted of two CPIES (Figure 1). After initial processing, described below, the PIES and CPIES produce daily observations of round-trip acoustic travel time, bottom pressure, and, for the CPIES, the velocity at 50 m above the seafloor. For the present study, the focus will be

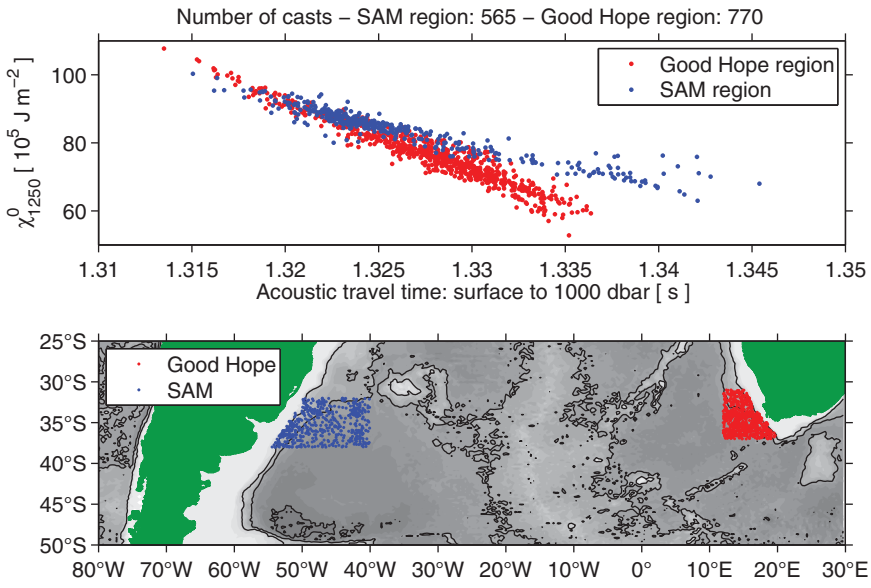

Figure 2. (top) Scatter plot illustrating the relationship between Fofonoff Potential (baroclinic stream-function) between the surface and 1250 dbar and the round-trip acoustic travel time between the surface and 1000 dbar. (bottom) The locations of the hydrographic (CTD and Argo) profiles used to make the top plot.

on the travel time and the bottom pressure measurements from the two instruments near the top of the continental slope: Site A located at approximately 1360 m depth on the western slope, and Site Z located at approximately 1005 m depth on the eastern slope (Figure 1).

[7] The bottom pressure sensors in the PIES collect hourly measurements, and the sensors are subject to exponential and/or linear drifts that must be removed prior to analysis [e.g., *Watts and Kontoyiannis*, 1997; *Donohue et al*., 2010]. In addition to this drift removal, the pressure sensor data were processed to remove strong tidal signals using a response analysis technique and then were low-pass filtered with a second-order Butterworth filter that has a 72 h cutoff period, passed both forward and backward to avoid phase shifting. The resulting records were subsampled to one value per day at noon UTC. The acoustic travel time measurements were also collected hourly. There is no drift or strong tidal signal in the travel time measurements, so they were filtered with the same Butterworth filter and subsampled to one value per day to focus on similar time scales. Analysis of the bottom pressure measurements is fairly straightforward, however the analysis of the travel time measurements requires some additional explanation.

[8] The earliest uses of IES involved comparing the travel time measurements to expendable bathythermograph (XBT) data in order to "calibrate" the travel time records into vertically integrated heat content [e.g., *Rossby*, 1969] or main thermocline depth [e.g., *Watts et al*., 1995]. Later research derived relationships between travel time and integrated quantities such as dynamic height [e.g., *Garzoli and Gordon*, 1996] using conductivity-temperature-depth (CTD) profiles from the region. In these studies, the CTD data were used to simulate travel times at a certain pressure level by vertically integrating the sound speed profile determined from the CTD measurements using the empirical sound speed equation [*Del Grosso*, 1974]. A key aspect of these methods for interpreting the travel time is that the relationships are determined purely from existing hydrographic observations in the region (which need not be contemporaneous with the moored observations). These integral quantity comparisons demonstrate the relationship between the travel time measurements and the baroclinic structure of the ocean.

[9] For the regions of the two pilot arrays used here, the hydrographic profiles can be used to demonstrate the strong relationship between the Fofonoff Potential [*Fofonoff*, 1962], which is also commonly referred to as the potential energy anomaly or baroclinic transport stream-function, and the simulated travel time (Figure 2). The Fofonoff Potential is essentially the vertical integral of the dynamic height anomaly. Differences in Fofonoff Potential between neighboring sites are directly proportional to the baroclinic component of the transport, relative to an assumed level of no motion [e.g., *Meinen and Watts*, 2000]. The relationship between Fofonoff Potential and travel time is used here mainly for estimating some of the errors inherent in the MOC calculations (see Appendix A). To analyze the PIES/CPIES data collected by the pilot arrays, Argo float profiles and CTD profiles spanning from the surface down to at least 1000 dbar in the regions illustrated in Figure 2 were collected from the Argo data centers, the World Ocean Database, and from recent cruises; a total of 565 profiles were available near the western array and 770 profiles were available near the eastern array. In order to study the MOC, the simple bulk transport integral over a particular depth range (such as the surface-to-1250 dbar Fofonoff Potential integration used for Figure 2) is not sufficient—and as such a more detailed analysis technique is required for the travel time data.

[10] *Meinen and Watts* [2000] developed a technique for estimating the full-water-column profile of density, rather than just the thermocline/pycnocline depth, integrated

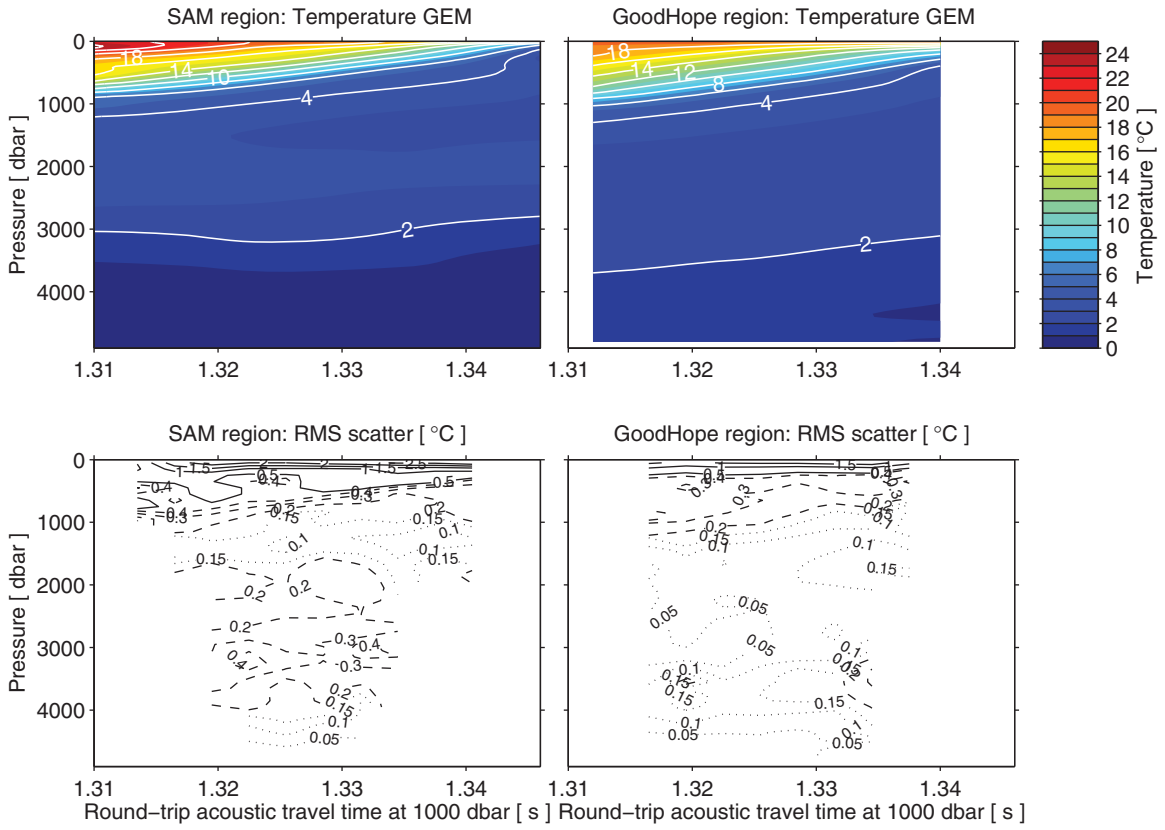

Figure 3. Gravest empirical mode (GEM) fields of temperature determined for the SAM and GoodHope regions (top left and right, respectively). Also shown are the root-mean-squared (rms) differences between the original hydrographic measurements and the smoothed look-up table values. Note in the lower plots the solid, dashed, and dotted contours represent progressively smaller contour intervals. The GEM fields were determined using the hydrographic profiles indicated in Figure 2.

Fofonoff Potential, or heat content, from the combination of IES travel time measurements and CTD data. Termed the "Gravest Empirical Mode," or "GEM," method, the analysis technique involves creating two-dimensional look-up tables of temperature, salinity, and/or density as functions of pressure and travel time. Figures 3 and 4 show the GEM temperature and salinity fields, respectively, for the western and eastern regions. The changes in vertical structure moving from the left side of the GEM fields to the right (or vice versa) demonstrate that these profiles do not represent a frozen-field simply shifting up and down, but instead are guided by the vertical structure inherent in the original hydrographic data and that they capture the water mass variability of the regions. A key strength of this technique is that it provides accuracy estimates directly from the scatter between the original hydrographic data and the smoothed look-up table values (Figures 3 and 4, bottom). While the profiles estimated via the GEM method do not have the water property accuracy of an actual CTD cast or dedicated temperature-salinity sensors on a tall mooring, they do capture the major water masses and they have been shown to be quite capable of accurately capturing volume transport fluctuations [e.g., *Meinen and Watts*, 2000; *Meinen et al*., 2004, 2013]. Combining the travel time measurements from a PIES/CPIES with the GEM look-up tables (e.g., Figures 3 and 4) produces daily full-water-column profiles of temperature, salinity, and density (or specific volume anomaly) at each PIES/CPIES site. In this paper, these estimated profiles are used to compute geostrophic velocity profiles that can be vertically integrated to help determine volume transport in the upper limb of the MOC.

[11] The final major data set used for this study is the Cross-Calibrated Multi-Platform (CCMP) wind product [*Atlas et al*., 2011], which merges the existing satellite scatterometer and microwave radiometer observations in a careful, internally consistent, manner and produces a gridded 6 h wind speed data set. For this preliminary analysis the 6 h CCMP wind speeds along 34.375°S, the grid line nearest to 34.5°S, were averaged to one value each day (Figure 5, top). Because the wind speeds in this region are not particularly strong (Figure 5, top), they were converted to wind stress using constant values of the drag coefficient, 1.43×10^{-3}, and air density, 1.225 kg m^{-3} following *Weisberg and Wang* [1997]. These wind stress values were then converted into Ekman transports via the standard method [e.g., *Emery and Thomson*, 1997] using the local Coriolis parameter and a constant seawater density of 1030 kg m^{-3}. The transports were integrated between Sites A and Z only, as the Ekman flows inshore of Sites A and Z are included in the model values which will be discussed shortly. The resulting mean Ekman transport integrated between Sites A and Z is +1.5 Sv ($1\ Sv = 10^6\ m^3\ s^{-1}$),

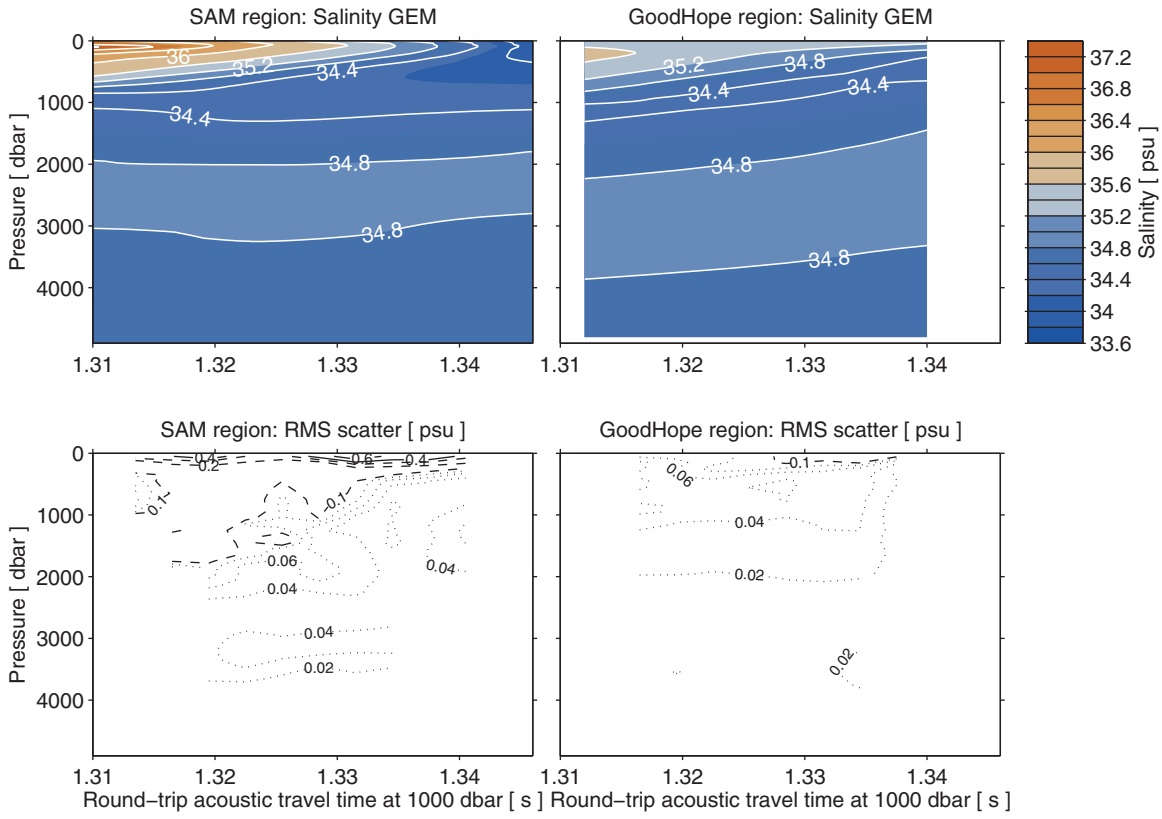

Figure 4. Same as Figure 3, except for salinity.

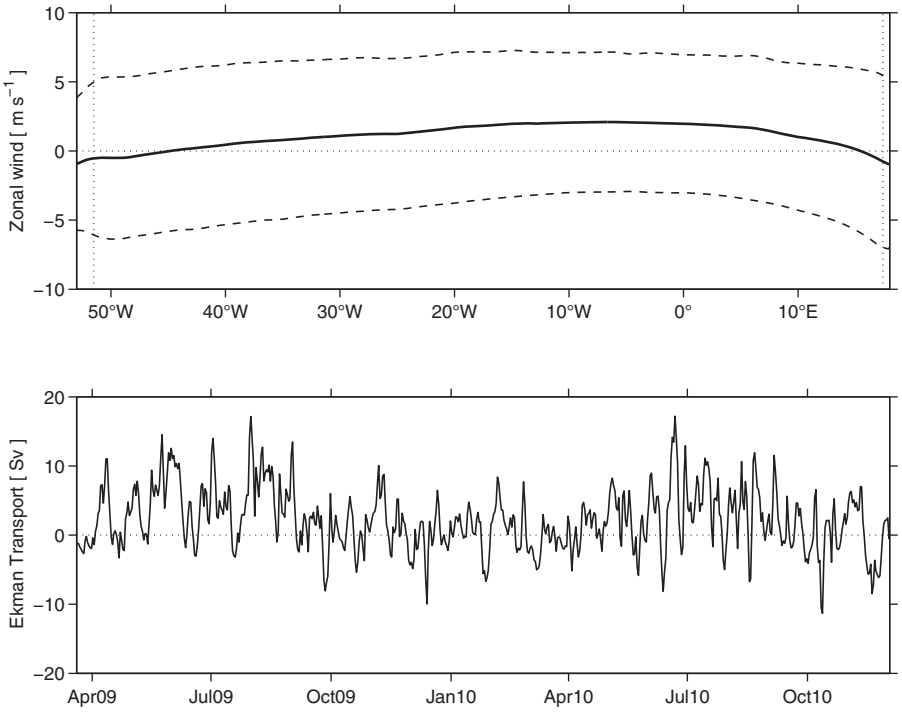

Figure 5. (top) Time-mean (solid line) plus/minus the standard deviation (dashed lines) of the zonal wind across 34.375°S (the nearest grid line to 34.5°S) determined from the CCMP wind product over the same time period as the pilot arrays. Vertical dotted lines indicate the locations of Sites A and Z. (bottom) Time varying meridional Ekman transports determined from the CCMP winds at the latitude of the pilot arrays and integrated from Site A to Site Z.

positive indicating northward, with daily values ranging from a peak southward value of −11.3 Sv to a peak northward value of +17.2 Sv (Figure 5, bottom); the range after a 10 day low-pass filter (not shown) is from −10.5 Sv to +13.6 Sv. The standard deviation of the unfiltered daily estimates over this time period is 4.3 Sv.

[12] These two pilot arrays were not initially designed to capture the complete MOC, but rather the near-boundary components of the MOC. In order to estimate the MOC with these data, it is necessary to use ancillary information. Clearly, the arrays miss the flows up on the relatively shallow continental shelves and the slope inshore of the shallowest PIES/CPIES sites located near the 1000 m isobath. Additionally, as will be discussed shortly, the array cannot directly measure the basin-wide average time-mean bottom velocity. To address these shortcomings for this analysis, the outputs from two numerical models were consulted (and the results are validated against other existing direct observations where possible).

3. Models

[13] The first model used to evaluate and improve the array estimates of the MOC is the Ocean general circulation model For the Earth Simulator (OFES) [e.g., *Sasaki et al*., 2008]. The OFES model is operated by the Japan Agency for Marine-Earth Science and Technology (JAMSTEC) and is a massively parallelized implementation of the National Oceanic and Atmospheric Administration/Geophysical Fluid Dynamics Laboratory (NOAA/GFDL) Modular Ocean Model version 3 (MOM3). The model equations have been discretized in a Mercator B-grid with a horizontal resolution of 0.1° and 54 vertical *z* levels. For the present analysis, model fields were provided by JAMSTEC in 3 day snapshot intervals on a 0.2° horizontal grid (i.e., every other grid point) from 1980 to 2006. The OFES model was spun up for 50 years with a monthly climatology derived from National Centers for Environmental Prediction-National Center for Atmospheric Research (NCEP/NCAR) reanalysis atmospheric fluxes [*Masumoto et al*., 2004], and then was forced with daily mean NCEP/NCAR reanalysis data from 1950 to 2006 [*Sasaki et al*., 2008]. To avoid initial spin-up transients, only the data from the final 27 years of the run were used for this analysis. Note that this model has previously been successfully validated against both other models and the limited available observations in the South Atlantic [e.g., *Dong et al*., 2011; *Perez et al*., 2011].

[14] The second model selected for this analysis is a global simulation based on the NEMO/OPA (Nucleus for European Modelling of the Ocean/Océan PArallélisé) numerical code [*Madec*, 2008]. The simulation was run and provided by the Mercator Océan project, the French center for ocean forecasting (www.mercator-ocean.fr). It is a global ocean/sea ice 1/12° horizontal resolution model configuration (ORCA12) operating on a tripolar ORCA grid type [*Barnier et al*., 2006]. This grid delivers a horizontal resolution of 9.25 km at the equator, 7 km at the latitude of the South Atlantic array (34.5°S), and 1.8 km in the Ross and Weddell Seas. The vertical grid is 50 *z* levels, with 22 levels stacked in the upper 100 m. The vertical resolution begins with 1 m at the surface and decreases to 450 m at the deepest levels. The ocean code is the NEMO version 3.2 [*Madec*, 2008], which resolves the primitive equations. The simulation starts on 1 October 1999 from rest with temperature and salinity climatological fields [*Levitus et al*., 2005], and ends 26 February 2007. The model is driven at the surface by the ERA-Interim reanalysis [*Dee et al*., 2011] at 3 h sampling for turbulent quantities (2 m surface air temperature and humidity and 10 m wind) and with daily means for radiative and precipitative fluxes. The bulk CORE formulation is used for turbulent exchanges [*Large and Yaeger*, 2009]. Only the final 6 years of the simulation are used to avoid initial transients.

4. Methods

[15] The strength of the MOC in the Atlantic Ocean is most commonly defined as the net basin-wide northward volume transport in the upper layer, i.e., integrated downward from the ocean surface to the depth where the net basin-wide flow transitions from northward to southward, neglecting occasional anomalous transitions within the Ekman layer [e.g., *Kanzow et al*., 2007; *Rayner et al*., 2011]. In essence, to determine the MOC transport a measure of the basin-wide integrated transport as a function of depth (or pressure) is required. For the 26.5°N array in the North Atlantic this is determined by summing the following transport components: the Ekman flow; the horizontally integrated geostrophic flow relative to an assumed level of no motion near the bottom, determined from the gradient between density profiles measured at the base of the western continental slope and at a set of short moorings that step up the eastern continental slope/shelf; and the flow on the western boundary, including the flow along the continental slope and the flow in the Straits of Florida, measured directly via current meters and a submarine cable, respectively. This sum is then adjusted to produce zero net volume transport across the section at time scales of 10 days and longer by applying a barotropic correction in the interior to address the assumed level of no motion [e.g., *Cunningham et al*., 2007; *Kanzow et al*., 2007].

[16] For the present study, a similar approach is adopted, with the basin interior flow being calculated geostrophically as the gradient between density profiles at Sites A and Z (Figure 1), and the Ekman transports calculated using the CCMP winds (Figure 5)—the same wind product used for the 26.5°N array analyses up through December 2011. There are, however, a few important differences in how the MOC is calculated here.

[17] First, due to the configuration of this pilot array, there is a lack of observations near the boundaries, and therefore the flows inshore of Site A in the west and of Site Z in the east cannot be directly estimated (see Figure 1). These flows are roughly an order of magnitude smaller than what is observed by current meters and the submarine cable at 26.5°N, but nevertheless they are not negligible. There is insufficient observational data available to determine the daily transports in these small regions at 34.5°S, however, the time-mean and standard deviations of the transports in these areas have been determined from three sources. The two numerical models discussed previously (OFES and NEMO) were used to estimate the transports inshore of Sites A and Z (Figure 6). The western and eastern inshore

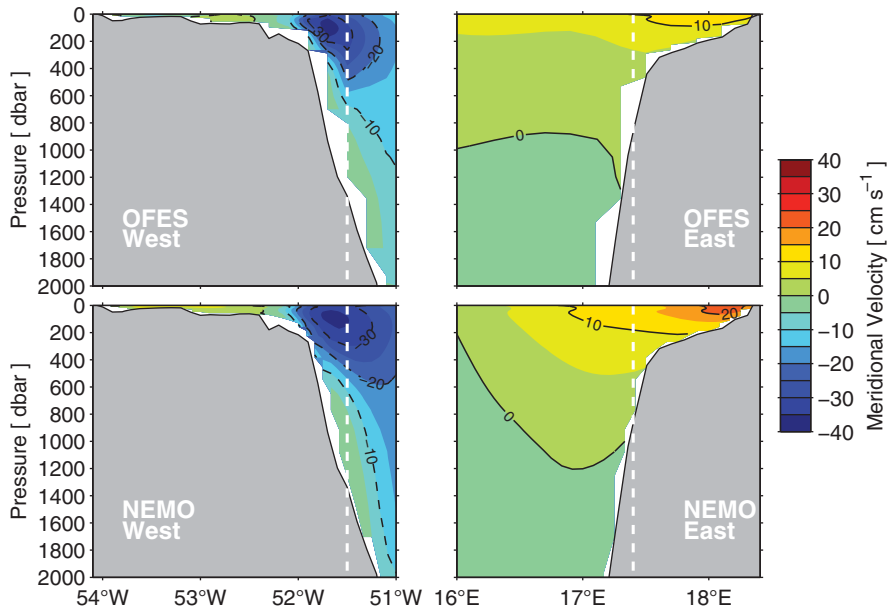

Figure 6. Time-mean meridional velocity on the western and eastern continental shelves and upper slopes at 34.5°S from (top) the 27 year run of OFES described in the text and (bottom) the 7 year run of NEMO described in the text. Gray shading indicates the ocean bottom. Vertical white dashed lines indicate the longitudes of Sites A and Z in the pilot arrays in the real ocean.

transports were, respectively, -3.0 ± 1.6 Sv and $+2.2 \pm 2.2$ Sv from the OFES run and -4.6 ± 3.3 Sv and $+4.1 \pm 4.7$ Sv from the NEMO run (time-mean ± one standard deviation). Additionally, repeated trans-basin XBT section data collected on a nearby transect [e.g., *Dong et al*., 2009; *Garzoli et al*., 2013] were used to estimate the inshore transports. Approximately 18 XBT sections were available along the nearby transect, and the western and eastern transports inshore of Sites A and Z were, respectively, -2.1 ± 2.5 Sv and $+1.2 \pm 0.8$ Sv (time-mean ± one standard deviation). As is discussed in Appendix A, transport by the unresolved eastern and western boundary flows largely cancel each other in the mean and using any of these three pairs of values in generating an MOC estimate results in time-mean MOC transports within approximately ±0.2 Sv of one another. The time-varying impacts (standard deviations) of these inshore flows are, however, a more serious consideration, as their time varying transports can be as large as 3–4 Sv. The circulation patterns associated with the flows not captured on the western and eastern boundaries are quite different. In the west, the array misses a portion of the Brazil Current core (Figure 6), inshore of which the flow on the relatively wide and shallow continental shelf is generally very weak. Previous high-resolution regional simulations have indicated only small (<0.5 Sv), seasonally reversing flows over the shelf [*Palma et al*., 2008], however the addition of a portion of the variability associated with the Brazil Current results in the higher variability inshore of Site A in the models and XBT data. By contrast, on the eastern boundary the bulk of the flow associated with the broad Benguela Current is offshore of Site Z; most of the flow not captured by the existing array on the east side occurs on the relatively narrow continental shelf and its transport is not distinguishable from zero (Figure 6). Because the actual daily time-varying transports inshore of Sites A and Z cannot be estimated with the existing data, the OFES mean inshore value is applied for the basin-wide MOC calculation, and these estimates of the standard deviations of the inshore transports will be considered as contributing to the accuracy estimates of the preliminary MOC time series (see Appendix A).

[18] The most important distinction between how the MOC is calculated in this study versus at 26.5°N is that at 34.5°S only the upper limb of the MOC is being directly measured—not the full depth profile. In some ways, this parallels the method applied in the MOVE array at 16°N, where only the lower limb of the MOC is directly observed [*Send et al*., 2011]. However, horizontally, the 34.5°S integration fully spans the basin aside from the continental shelves and uppermost slopes, whereas at 16°N the MOVE array only spans from the western boundary to the Mid-Atlantic Ridge. Note also that the 34.5°S arrays do have measurements in the deep layers from the other sites—however one of the key locations, Site B, had an electronics failure during a significant portion of the overlapping period of the two arrays, preventing its use for this study and limiting the ability to measure the basin-wide deep flows during this time period. As will be discussed shortly, the PIES/CPIES bottom pressure records at 34.5°S are coupled with the time-mean basin-wide averaged OFES velocity at 1350 dbar to estimate an absolute velocity reference for the relative geostrophic velocity profiles. As a result, the transport-per-unit-depth profiles calculated here are absolute, not relative to an assumed level of no motion. Therefore, this method only needs to produce transport-per-unit-depth profiles from the surface down to the depth where the transport changes from northward to southward, and it has the advantage of proceeding without the need for a zero-net-volume-transport correction. It must be noted, however, that this method has its own limitations.

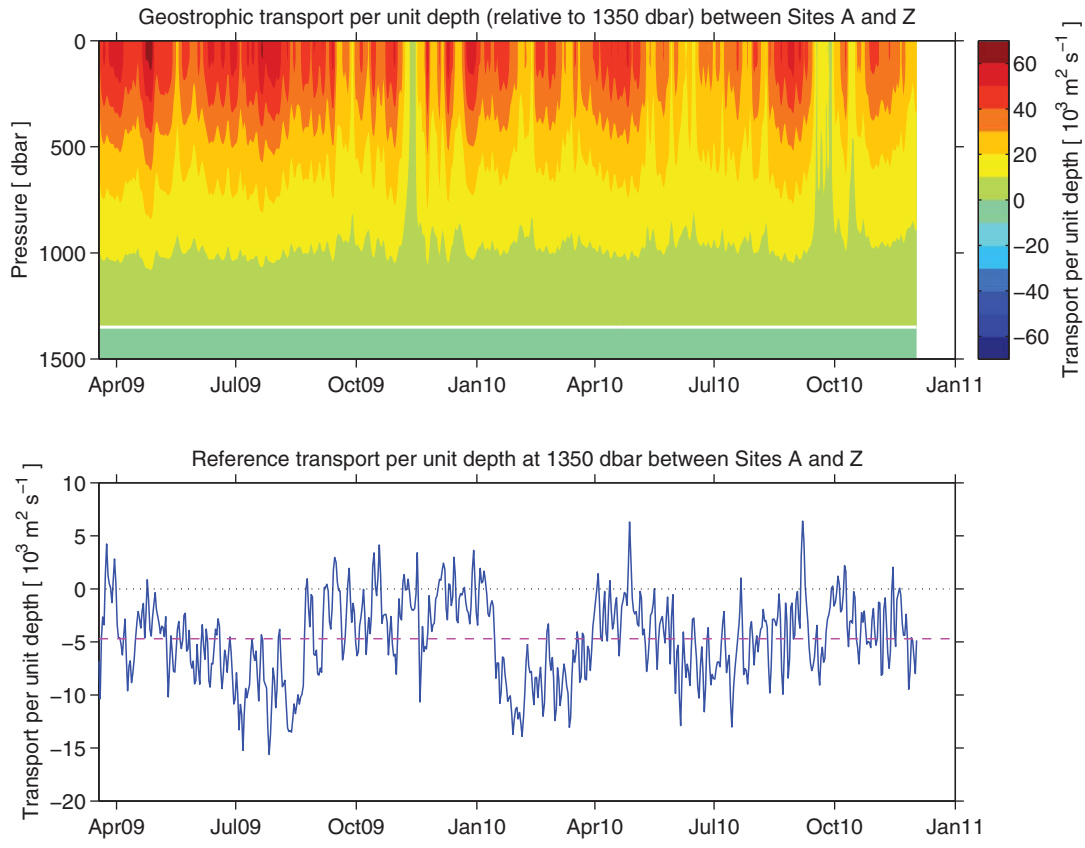

Figure 7. (top) Time/pressure plot of the geostrophic transport per unit depth, relative to 1350 dbar, integrated between Sites A and Z. Zero transport is indicated by the white horizontal contour at 1350 dbar. Positive values indicate northward flow. (bottom) Absolute reference transport per unit depth determined from the pressure records at Sites A and Z. As noted in the text, the time-mean reference transport is determined from the 27 year OFES run (magenta dashed line in the figure). Zero transport is shown by the black dotted line.

[19] The aforementioned PIES/CPIES-estimated density profiles can be vertically integrated to yield profiles of dynamic height anomaly (geopotential height anomaly). Differencing dynamic height anomaly profiles between two PIES/CPIES sites gives the component of the geostrophic velocity orthogonal to the line between the sites, relative to an assumed level of no motion. This geostrophic velocity is a true integral of the motion between the two sites, and as such, differencing the dynamic height anomaly profiles at Sites A and Z (see Figure 1) yields the meridional geostrophic velocity, relative to an assumed level of no motion, averaged across nearly the entire basin. For this study, the level of no motion selected was 1350 dbar, which is close to the nominal depth of Site A. The final results are not particularly sensitive to choices within ±200 dbar; see Appendix A for an estimate of the small errors that are introduced because Site Z is located at a slightly shallower depth than Site A. The resulting velocity profiles can then be zonally integrated (multiplied by the basin width between Sites A and Z) to yield a profile of the basin-wide transport per unit depth relative to an assumed level of no motion at 1350 dbar (Figure 7, top).

[20] While the PIES/CPIES travel time measurements provide the geostrophic velocity profiles relative to an assumed level of no motion, as mentioned above the bottom pressure measurements can provide the reference velocity needed to make those relative geostrophic velocities absolute. Differencing bottom pressure measurements at the same geopotential surface from two different locations yields the absolute horizontal geostrophic velocity orthogonal to the line between those two sites [e.g., *Donohue et al*., 2010; *Meinen et al*., 2012]. Of course no two moorings can ever be deployed at exactly the same depth—particularly not relative to a constant geopotential surface. As such, the time-mean velocity between the two instruments cannot be ascertained from the bottom pressure records alone; this is commonly known as the "leveling" problem [e.g., *Watts and Kontoyiannis*, 1990; *Donohue et al*., 2010]. Note that the leveling problem applies only to the record-length time-mean, not to the time variability. The time-mean is not the focus of this study. Nevertheless, three estimates of the time-mean basin-wide average velocity were tested for combining with the time-varying absolute velocity reference at 1350 dbar. Two were based on time-mean basin-wide averages from the OFES and NEMO model runs discussed previously. The third mean velocity was from a gridded three-dimensional velocity product based on Argo float density profile measurements merged with Argo float drift velocities and satellite altimetry measurements (C. Schmid, personal communication, 2013).

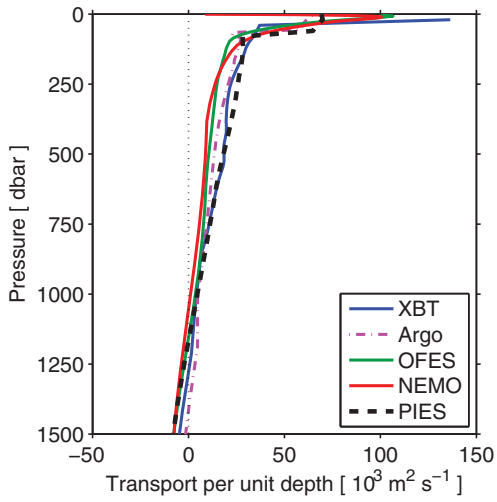

Figure 8. Estimates of the basin-wide transport per unit depth at 34.5°S—with the primary data set used in each estimate noted in the legend. Analysis methods for each estimate are described in the text. Note the structure differences in the upper ∼60 m are primarily due to how the Ekman transport is distributed over the Ekman layer in the different calculations; these structural differences are arbitrary and are not important for the present volume transport study.

The OFES, NEMO, and Argo/altimeter time-mean basin-wide average meridional velocities at 1350 dbar were -0.0007 m s^{-1}, -0.0009 m s^{-1}, and -0.0004 m s^{-1}, respectively. As is discussed in more detail in Appendix A, the differences between these three mean velocities are quite small, and they translate to time-mean differences in the MOC of less than ± 1.5 Sv. Once the time-mean is added to the time-varying reference velocity from the bottom pressure gauge differences, the result is a velocity that can be integrated (multiplied by the basin width) to yield the basin-wide averaged transport per unit depth at the reference level of 1350 dbar (Figure 7, bottom).

5. Results

[21] Combining the geostrophic transport per unit depth relative to the level of no motion at 1350 dbar ($T_{relative}(p, t)$; see Figure 7, top) with the absolute transport per unit depth at the reference level ($T_{reference}(t)$; see Figure 7, bottom) yields profiles of the absolute transport per unit depth integrated between Sites A and Z. Coupled with the Ekman transport ($T_{Ekman}(t)$; see Figure 5) and the time-mean inshore transports ($T_{inshore}(p)$; see Figure 6), the result is the total transport per unit depth as a function of pressure and time ($T_{total}(p, t)$; see Figures 8 and 9). Mathematically the basin-wide-integrated transport per unit depth can therefore be written as

$$T_{total}(p,t) = T_{relative}(p,t) + T_{reference}(t) + T_{Ekman}(t) + T_{inshore}(p)$$

where the terms are as defined above and the dependent variables "p" and "t" refer to pressure and time, respectively.

[22] The time-mean structure of $T_{total}(p, t)$ is as expected (Figure 8), with northward flow in the upper layer, particularly intensified in the Ekman layer, and southward flow at depth. The time-mean transition from positive (northward) to negative (southward) flow occurs at roughly 1170 dbar, which is slightly shallower than but very close to what was found in an earlier published analysis of 27 snapshot XBT sections at about the same latitude (1250 m) [*Garzoli et al.*, 2013] and to a previous inverse analysis estimate from a trans-basin CTD section in the region (∼1200 m) [*Saunders and King*, 1995]. The transition in the OFES model is essentially the same (∼1155 dbar), while in the NEMO model is it somewhat shallower (∼1080 dbar). In an Argo-based MOC product presently being developed by some of the authors, the transition is somewhat deeper (∼1400 dbar). Given the high degree of temporal variability observed in this transition depth (white contour in Figure 9), these small differences are not statistically significant. The observed time-mean transition depth from the PIES at 34.5°S is slightly deeper than the transition observed at 26.5°N (∼1100–1160 dbar) [see *Cunningham et al.*, 2007; *Kanzow et al.*, 2007].

[23] Estimates of the time-mean transport per unit depth have been made with several other data sets from previous studies near 34.5°S (Figure 8) that can be compared with the results obtained from the PIES data. There are some differences in the (arbitrary) depth layer into which the Ekman layer is inserted (upper 20–60 dbar, depending on the study; 60 dbar was used herein), however these differences are not important for the MOC volume transport calculation. (Note that these differences are very important to heat transport calculations, but that is beyond the scope of the present study.) The overall structure of the profiles is very similar. The XBT MOC estimate is an average of only those sections that most closely followed the 34.5°S track [see *Garzoli et al.*, 2013 for a discussion of the different tracks taken by the XBT vessels]. The Argo MOC profile shown in Figure 8 and discussed briefly in the previous paragraph is from an estimate presently under development by some of the authors using as its principal data set a climatology of all Argo float data collected up through mid-2012 in a band along 34°S, together with wind estimates and historical hydrographic climatology data near the shallow boundaries and below 2000 dbar. As noted above, the OFES and NEMO mean profiles are also similar, although they exhibit consistently weaker northward flow in the pressure range from roughly 100 dbar to 600 dbar. Overall though, the time-mean profiles from all five sources are quite similar—which might be as expected because the structure of the time-mean transport per unit depth profile is essentially set by the time-mean density gradient across the basin (aside from the Ekman layer). Because the models start up from a hydrography-based climatology, and because to a lesser or greater extent the XBT, Argo and PIES/CPIES methods all depend on historical temperature-salinity data, the mean density gradient for all of them is based mostly on the same historical data, so they should all produce the same time-mean transport-per-unit-depth profile. Note that if either of the models exhibited a significant drift in their temperatures and/or salinities over time, or if the climatology used to spin up either model had a significantly different temperature/salinity structure than the

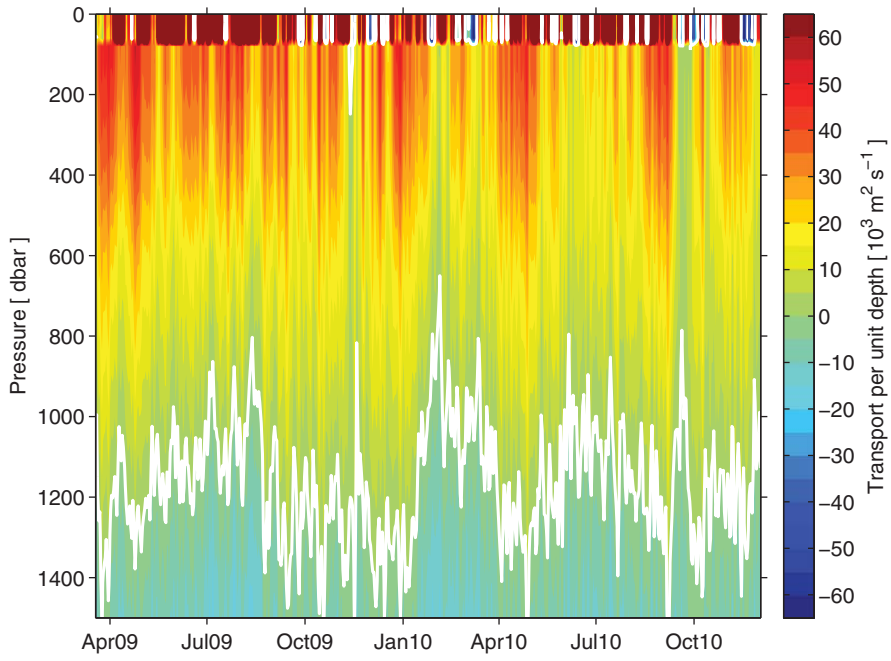

Figure 9. Hovmoller plot of the basin-wide absolute total (geostrophic plus Ekman plus shelf) transport per unit depth as a function of time. White contour indicates zero flow. Ekman transports have been applied uniformly over the upper 60 dbar of the water column.

modern CTD and Argo data, then of course the resulting mean from the models could be affected. The good agreement between models and observations here suggests that these two models have not drifted sufficiently from their initial conditions to result in a major change in the time-mean transport per unit depth profile, and that those initial conditions must have been similar to that observed in the modern CTD and Argo data.

[24] The transport-per-unit-depth profiles are quite variable in time (Figure 9), with the strongest northward flows typically found above about 500–600 dbar. The transition from northward to southward flow (white contour in Figure 9) ranges between 650 dbar and 1660 dbar, with a standard deviation of 150 dbar. There are sporadic short-lived weak-transport events, where the northward-southward transition shoals and the northward transports become lower, throughout the record, with events occurring in September 2009, November 2009, January 2010, and September 2010, for example. Evaluation of maps of AVISO gridded satellite altimeter data during these events (not shown) indicates that these low events are not simply associated with strong flows missed inshore of Sites A and Z. Evaluating the structure of the time varying flows through an Empirical Orthogonal Function analysis indicates that the transport variations are dominated by fluctuations which have a vertically sheared, surface intensified structure roughly similar to the shape of the classical first baroclinic mode, albeit with a nonzero vertical mean (not shown).

[25] Integrating these transport-per-unit-depth profiles ($T_{total}(p, t)$) down from the surface to the reversal in flow yields the time series of the MOC transport at 34.5°S (Figure 10). Some of the apparent low transport events in the profiles (Figure 9) appear clearly as net low MOC events (Figure 10; e.g., November 2009, September 2010), while others represent smaller overall decreases (e.g., September 2009). During the most extreme low events, the MOC upper layer transport drops to essentially zero, whereas during the largest high events the MOC daily transport reaches nearly 50 Sv. After the application of a 10 day low-pass filter (not shown), the range in MOC transports spans from 3 Sv to 39 Sv. This total MOC variability is essentially the sum of the geostrophic relative transport, the absolute reference transport, and the Ekman transport. Evaluating the correlation coefficients between these various components and the total MOC (respectively, $r = 0.73$, $r = 0.33$, and $r = 0.56$) indicates that the geostrophic relative transport dominates the total, explaining about 53% of the total variance, while the Ekman (∼31%) and reference velocity (∼11%) are lesser, but not trivial, contributors. The observed integral time scales [e.g., *Emery and Thomson*, 1997] for the three terms are quite different, with the relative geostrophic transport, absolute reference transport, and Ekman transport terms having integral time scales of 20 days, 12 days, and 8 days, respectively. This suggests that the Ekman role is at the higher end of the frequency spectrum, while the relative geostrophic transport term varies somewhat slower. The amplitudes (standard deviations) of the terms are all comparable, ranging from 4.5 Sv for the Ekman transport to 5.9 Sv for the relative geostrophic transport term (the absolute reference transport term is 5.2 Sv). The total MOC has a standard deviation of 8.7 Sv, which is likely a bit artificially high due in part to missed variability on the upper continental slopes and shallow shelves (e.g., eddies that are only partially observed within the array, with the other compensating portion of the eddies unobserved inshore of the array). There is no meaningful correlation between the MOC observed at 34.5°S and that at 26.5°N (correlation coefficient $r = 0.06$), and there are

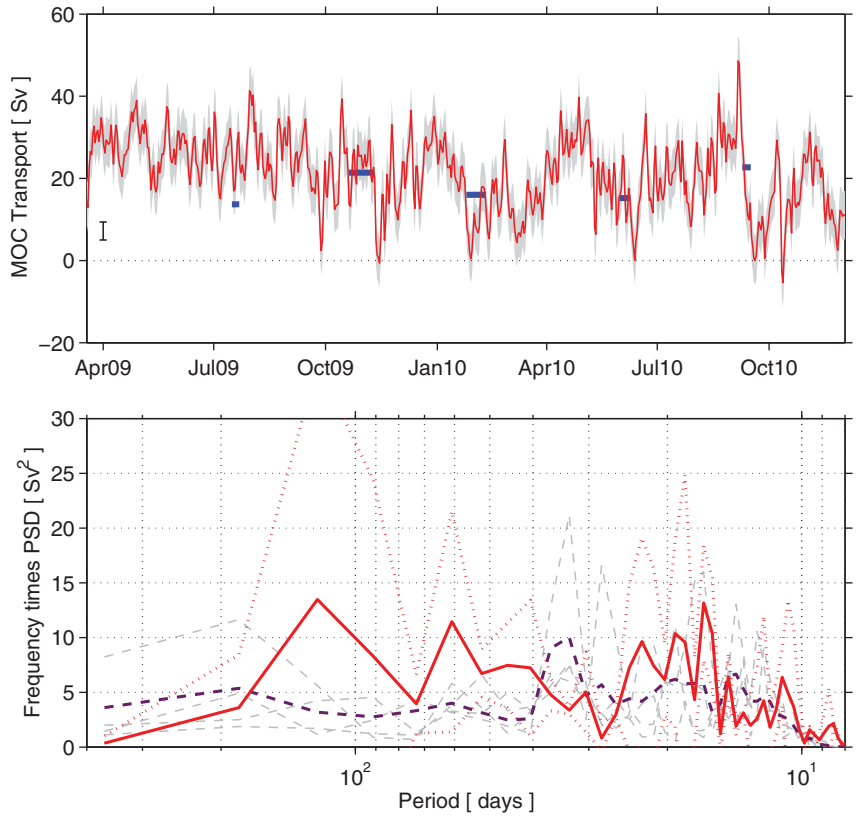

Figure 10. (top) Transport time series of the MOC at 34.5°S (red line) with estimated daily error bars (gray shading) as derived in Appendix A. Black vertical error bar at left illustrates the estimated bias accuracy as discussed in the Appendix A. Also shown are five MOC estimates determined from trans-basin XBT sections where the horizontal length of the bar illustrates the start and end times of each trans-basin cruise. (bottom) Variance preserving spectrum of the MOC transport time series (red solid line) calculated using a 1 year window with 50% overlap. Also shown are the 95% confidence limits (red dotted lines). Thin gray dashed lines show spectra of the MOC at 26.5°N for comparison using four 623 day long segments of the complete record; thick purple dashed line shows the spectrum for the complete 7 year record at 26.5°N.

no obvious events that coexist during the ∼20 months of overlap in the two records (not shown). This is consistent with there being a lack of meridional coherence in observed MOC time series at different latitudes, although the ∼20 month record at 34.5°S is too short to make definite statements regarding coherence at time scales longer than perhaps 3–6 months or lagged correlations that may exist at lags longer than can be evaluated with the short record.

[26] The spectrum of the total MOC at 34.5°S (Figure 10, red line in bottom) indicates that there is energy at the 16–25, 60, and ∼110 day time scales, however the estimated error bars on the spectra (Figure 10, red dotted lines in bottom) grow quite wide at longer periods, illustrating the limitations of studying time scales longer than ∼50–60 days with a ∼600 day long record. For comparison, the spectra of the first ∼7 years from 26.5°N (Figure 10, purple line in bottom) is at roughly the same energy level through the shorter periods but is generally below the 34.5°S spectra at periods greater than 50–60 days (but well within the projected error bars for the 34.5°S spectrum at those longer periods). Also shown are spectra from the 26.5°N array using five different 623 day subsets of the full record (Figure 10, gray dashed lines in bottom). These spectra illustrate the widely different longer period variability that one can observe from one segment of the record to the next, and demonstrate the need for caution that must be used in interpreting the longer period portion of the spectra.

[27] The only concurrent, independent, in situ data set available for comparison to the daily time varying MOC at 34.5°S comes from five XBT sections along what is called the "AX18" line between Cape Town, South Africa, and Buenos Aires, Argentina [e.g., *Baringer and Garzoli*, 2007; *Garzoli and Baringer*, 2007; *Dong et al.*, 2009; *Garzoli et al.*, 2013]. Unfortunately, due to logistics problems with the volunteer deployment vessels, only one of the five sections during 2009–2010 was along the proper AX18 line (May–June 2010), while for the others the west end of the transect was shifted significantly northward to Santos, Brazil (∼24°S, called "AX18*"). Previous analysis using output from the OFES model has suggested that while changing the western endpoint from Buenos Aires to Santos has a significant impact on the meridional heat transport across the transect, the impact on volume transport is negligible [*Garzoli et al.*, 2013]. Irrespective of whether the XBT section was along AX18 or AX18*, the XBT-derived MOC values generally overlap the

Table 1. Comparison of PIES/CPIES and Concurrent XBT MOC Transports[a]

Dates of XBT Cruise	XBT MOC Estimate	Mean PIES MOC Estimate During Cruise	STD PIES MOC Estimate During Cruise	Peak-to-Peak Range of MOC Estimates During Cruise
16–22 Jul. 2009	13.7 Sv	23.4 Sv	5.3 Sv	17.0–31.3 Sv
20 Oct. to 10 Nov. 2009	21.4 Sv	22.8 Sv	4.4 Sv	13.2–29.3 Sv
25 Jan. to 10 Feb. 2010	16.0 Sv	9.6 Sv	5.6 Sv	0.4–18.0 Sv
31 May to 9 Jun. 2010	**15.2 Sv**	**16.3 Sv**	**5.5 Sv**	**9.3–25.6 Sv**
9–16 Sep. 2010	22.7 Sv	15.1 Sv	6.8 Sv	6.0–27.2 Sv

[a]Note that the XBT sections take 1–3 weeks to complete, depending on the vessel and the weather. The cruise highlighted in bold (May/June 2010) is the only cruise completed upon the "AX18" track that most closely approximates the latitude of the pilot mooring arrays—see the text.

PIES/CPIES-derived MOC time series at some point during the time period of the transect (Figure 10, blue bars in top; see also Table 1). The variability exhibited in the PIES/CPIES MOC time series during the time period when each XBT section was collected is quite significant, with temporal standard deviations of 4.4–6.8 Sv over the roughly one to 3 week period of each cruise (Table 1). Optimistically one could argue that, aside from the earliest cruise, because the PIES/CPIES MOC transport time series intersects the XBT section MOC transport at least once during each cruise that the sections and moored time series are in almost perfect agreement. More realistically, the large temporal variations observed during the sections illustrate the asynopticity inherent in collecting trans-basin hydrographic sections of any kind. It is impossible to ascertain with the existing data precisely how much of the difference between the XBT MOC estimates and the PIES/CPIES transports averaged during the XBT sections can be explained due to asynoptic errors in the section estimates. It is possible, however, to estimate the accuracy of the PIES/CPIES MOC estimates.

[28] Because the method for calculating the MOC presented in this study does not use a "residual" type correction for constraining zero-net-volume-transport across the section, the transport accuracy can be determined simply by evaluating the accuracies of the various measurement systems (and adding the errors associated with the estimated inshore variability missed by the arrays). The details of the "error bar" derivations are left to Appendix A; based on a careful evaluation of the potential sources of error, the daily MOC transports presented herein are estimated to be accurate to within 5.9 Sv (with no low-pass filtering applied), while the various potential sources of time-mean bias error in the calculations could yield time-mean offsets of up to 4.4 Sv. Because the XBT MOC estimates are made using a residual-type method [e.g., *Dong et al*., 2009; *Garzoli et al*., 2013], they do not have a similar type of formal measurement accuracy. Nevertheless, adding the PIES/CPIES estimated error bars to the observed MOC time series (gray shading in the top of Figure 10) demonstrates that the XBT observations are all within the expected window of the PIES/CPIES error estimates alone in all cases.

[29] As an aside, it is possible to evaluate at least one component of the error bars on the XBT MOC estimates using the PIES/CPIES data. Under the assumption that the PIES/CPIES MOC estimates are perfect, the time variability of the PIES/CPIES estimates during the XBT transects provides some estimate of the asynoptic errors in the XBT sections. Averaging the observed standard deviations (STD; Table 1) during each of the five XBT transects gives an average temporal standard deviation of about 5.5 Sv. If this value is taken to be a "worst case," or very conservative, measurement accuracy for the XBT section MOC estimates (basically assuming that all other sources of error would be smaller than the asynopticity error), then the observed differences between the XBT and PIES/CPIES MOC estimates are well within the combined error bars of the two types of estimates.

6. Discussion and Conclusions

[30] The lack of clear correspondence between the 34.5°S spectrum and the 26.5°N spectrum (Figure 10, bottom) leads one to question whether the dynamics driving MOC variations at relatively short periods (annual or less) are different at the two latitudes. A detailed analysis of this issue cannot be completed with the limited record to date at 34.5°S, however some important information can be gleaned from the existing ~20 month time series.

[31] The variability of the observed MOC is, by nature of the way it is calculated, due to variations in either the Ekman transport, in the "barotropic" reference flow added at 1350 dbar, or to the "baroclinic" relative velocity profiles determined from the density profiles on either side. Perhaps the easiest way to determine the contribution that these terms make is to calculate the difference between the observed MOC and a "simplified MOC" which would be determined if a term such as the Ekman transport was held constant in time; the difference between these MOC estimates will be the impact of a specific term on the total MOC (Figure 11). The contributions of the Ekman, reference and relative terms (Figure 11—red, green, and blue lines, respectively) are quite variable at a range of time scales, with variations of 10 Sv or larger persisting at times for 2–3 weeks and variations of 3–5 Sv sometimes lasting for months. The story these time series tell is clearly quite complicated, but some of the strongest MOC signals can be ascribed to specific terms. The strong 2–3 week low MOC event that occurs in November 2009, for example, is clearly associated with a change in the relative transport, whereas the abrupt low and then high MOC events that occur in June 2010 are primarily due to changes in the Ekman transport. Other events, such as the 5–10 Sv high MOC period in April–May 2010, appear to be the superposition of positive contributions from more than one of the terms.

[32] One of the many interesting results that have come from the 26.5°N array is the fact that the annual variations of the MOC at that latitude are driven by fluctuations in the density profile at the eastern boundary [*Chidichimo et al*., 2010]. These density fluctuations at 26.5°N appear to be

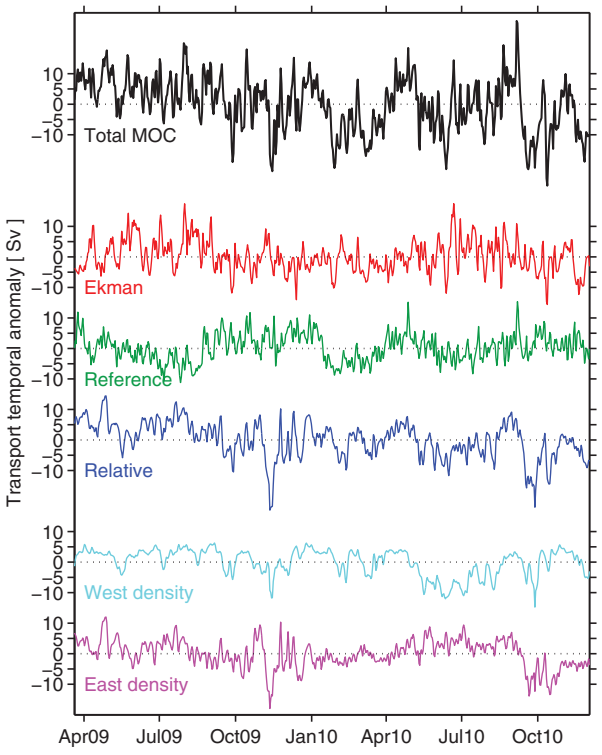

Figure 11. Time variability of various contributors to the total MOC (determined as described in text), with the time-means removed. Black bold line indicates the total MOC (as in Figure 10), while the red, green, and blue lines each represent, respectively, the contribution to the MOC made by the Ekman transport, the 1350 dbar reference velocity transport, and the geostrophic transports relative to zero flow at 1350 dbar. The light blue and magenta lines, respectively, indicate the contributions to the relative transport when either the west side density profile at Site A (light blue line) or east side density profile at Site Z (magenta line) are held constant.

driven primarily by changes in the wind stress curl at the eastern boundary [*Kanzow et al.*, 2010]. With only ∼20 months of data collected to date, it is somewhat premature to interpret the annual time scale at 34.5°S, however a similar breakdown of the western and eastern contributions to the relative transports at 34.5°S can still be evaluated at the range of shorter time scales available. A similar technique to that described above, holding either the west side (Site A) or east side (Site Z) density profiles constant when computing the relative transport term and then determining the difference between this "simplified" MOC estimate and the actual MOC time series isolates the contribution of each density profile. The east side density (Figure 11—magenta line) appears to have a bit more high-frequency variability in it (periods of ∼1 week), whereas the west density variations appear strongest at slightly longer periods, perhaps 3+ weeks. The variations induced by the east density are also generally of larger magnitude, in some cases exceeding 20 Sv peak-to-peak. The very low MOC event in November 2009, which as noted earlier was primarily associated with the relative transport term, is clearly driven by the variation in the east side density (Figure 11—magenta line), although interestingly the west side has a weak sympathetic variation at the same time. A similar event is observed in late September 2010. In general the density contributions from the west and east side are uncorrelated ($r = -0.07$). Overall the west and east density variations have a roughly equal impact on the variability of the relative transport term (correlations of $r = 0.66$ and $r = 0.70$, respectively).

[33] The coherence between these "simplified MOC" estimates and the complete MOC estimate provides a bit more detail than the simple correlation. Because of the time series length (∼20 months), statistically significant coherences are only found at time scales shorter than about 90 days regardless of which of the time series are being compared (Figure 12). Essentially, coherences that fall below the gray solid and dashed lines in Figure 12 are not statistically different from zero at the stated confidence levels and should not be considered for interpretation. The time scales where meaningful coherences are found,

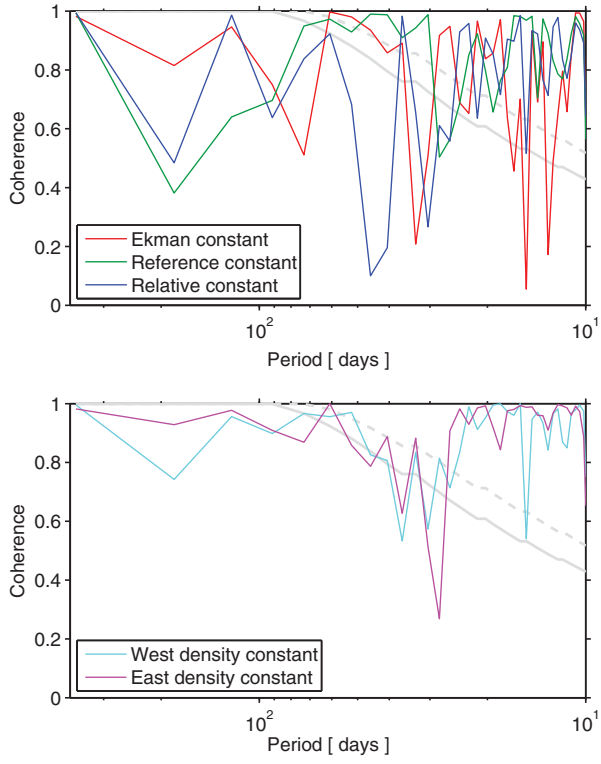

Figure 12. Coherences between the observed MOC and the MOC determined under various assumptions. (top) Coherence between the observed MOC and the MOC determined when either the Ekman transport, the reference velocity at 1350 dbar, or the geostrophic transport relative to 1350 dbar are held constant. Low coherence indicates that the term that was held constant plays a significant role in the variability of the MOC at that time scale. (bottom) Coherence between the observed MOC and the MOC determined when holding either the west side (Site A) density profile constant or the east side (Site Z) density profile constant. In both plots, the gray solid and gray dashed lines indicate the 95% and 99% significance levels for the coherences, respectively for the coherences, respectively, calculated following *Thompson* [1979].

periods <90 days, are also the time scales where most of the energetic fluctuations are observed in the ~20 month record (Figure 10, bottom). The individual lines plotted in Figure 12 are the coherence between the complete MOC and a "simplified MOC" where one term has been held constant in time; for example, an MOC calculated using a constant Ekman transport equal to the time-mean Ekman transport over the ~20 month time series. A high coherence at a particular period (or frequency) indicates that the term being held constant is not particularly important to the complete MOC at that period, because the simplified estimate that neglects that term is still varying consistently with the actual complete MOC. Lower coherences, by contrast, suggest that the term held constant plays a significant role in the total MOC at that time scale, because the simplified MOC that neglects that term no longer varies consistently with the complete MOC.

[34] The resulting coherences are fairly noisy, due to the short time series length, however it is clear that at periods of 10–20 days the Ekman contribution is much more important to the total MOC variability than the relative or reference terms (see the red line well below blue and green lines in Figure 12, top). For most periods between 20 and 40 days the relative flow appears to be equally, or perhaps slightly more, important to the total MOC than the Ekman flow. At periods between about 40 and 60 days the relative term clearly dominates the MOC variability with little input from the other terms. And at periods greater than 60 days all three terms appear to play a significant role, with the reference term possibly being the most influential at periods exceeding 100 days (although due to the record length the statistics are marginal at those periods).

[35] As far as the contributions of the two boundaries to the relative flow, in general the simplified MOC estimates holding alternately the western or eastern boundary density profiles constant are quite similar, with arguably the western boundary perhaps playing a slightly larger role at periods under 20 days and beyond 100 days (light blue line below magenta line in Figure 12, bottom). There are no periods where the east side density variability clearly dominates the relative term aside from right at 10 days and in a narrow range of periods near 25–30 days.

[36] The time-mean MOC transport estimate from the pilot arrays, 21.3 Sv, is less robust than the time variations due to the dependence on the numerical model time-mean as discussed previously. Nevertheless, it is reasonably close to previous mean MOC estimates determined from repeated XBT sections, e.g., 17.9 Sv [*Dong et al*., 2009] or 18.1 Sv [*Garzoli et al*., 2013], and an inverse estimate of 20 Sv that was made at 32°S [*Fu*, 1981]. The MOC variability estimates from these initial pilot arrays indicate that the MOC is just as variable at 34.5°S as has been observed in the North Atlantic at 16°N, 26.5°N, and 41°N. Comparing the published temporal standard deviations of the MOC volume transport at the various latitudes is somewhat complicated because the previous papers have all used different low-pass filter periods for their data. To facilitate comparison, the MOC transport time series presented herein has been low-pass filtered with cutoff periods of 10 days, 90 days, and 120 days and the standard deviation has been calculated for each filtered version of the record (Table 2). Comparing these standard deviations to those determined at other latitudes, the longest period MOC variability (120 day low-pass) is essentially the same (3.6–3.9 Sv) at the three latitudes where it is available (34.5°S, 16°N, and 26°N; see Table 2). With a cutoff period of 90 days, the standard deviation of the time series at 34.5°S is noticeably higher than at the other latitudes where it is available (26°N and 41°N), which is also true when a cutoff period of 10 days is used (only available at 26°N). The length of the records at the four different latitudes is very different (~20 months at 34.5°S versus 7+ years at the North Atlantic locations), so some caution in comparing the variability estimates is warranted. That having been said, as noted earlier the higher standard deviation at 34.5°S is most likely at least partially due to the standard deviation at 34.5°S being artificially increased due to missed compensating variability on the continental shelves (e.g., eddies only partially captured between Sites A and Z, with their opposite-signed counter-flow unobserved inshore). This phenomenon has previously been observed at 26.5°N [*Kanzow et al*., 2009]; the fact that the 120 day low-pass filtered records have a similar standard deviation is consistent with part of the higher frequency difference being due to eddy-like flows that are partially missed inshore of Sites A and Z. The accuracy of the estimates at 34.5°S from the pilot arrays is also not as good as that of the true full-depth trans-basin array at 26.5°N (see Appendix A). Nevertheless, the accuracy of the MOC estimates at 34.5°S is definitely sufficient to have demonstrated the crucial roles that the Ekman, reference, and relative contributions make to the total flow, as well as the importance of measuring the density variability on both boundaries (Figures 11 and 12).

Table 2. Standard Deviation of the MOC Volume Transport at the Indicated Latitudes After Low-Pass Filtering at Various Periods[a]

	Low-Pass Filter Periods			
Latitude of MOC Observation	No Filter	10 Days	90 Days	120 Days
41°N [*Willis*, 2010]			**2.4 Sv**	
26°N [*Cunningham et al*., 2007]		**4.9 Sv**	3.7 Sv	3.6 Sv
16°N [*Send et al*., 2011]				**3.8 Sv**
34.5°S [This study]	8.7 Sv	7.6 Sv	4.5 Sv	3.9 Sv

[a]Bold standard deviation estimates were published in the listed papers—the other estimates at 26°N were determined using the 26°N MOC time series for 2004–2011 (available from www.noc.soton.ac.uk/rapidmoc/). The final row shows the standard deviation results for the present study at 34.5°S for comparison.

[37] The results of these pilot arrays, coupled with previous modeling analyses [e.g., *Perez et al*., 2011] and XBT section analyses [e.g., *Baringer and Garzoli*, 2007; *Garzoli and Baringer*, 2007; *Dong et al*., 2009; *Garzoli et al*., 2013] show that a more complete trans-basin array at 34.5°S could accurately measure the MOC and will likely yield interesting contrasts to the North Atlantic MOC time series. Theoretical studies [e.g., *Dijkstra*, 2007; *Drijfhout et al*., 2011] have demonstrated that measurements of the MOC, and the associated salt fluxes, in this region will be crucial for understanding of the stability of the Atlantic MOC system. Planned further developments of the trans-basin array will provide the ability to calculate these

"higher-order" quantities like baroclinic salinity flux through better resolved horizontal velocity information and coupling with other existing data sets like the Argo profiling float array. The western boundary observations have already demonstrated significant variability in the Deep Western Boundary Current, carrying part of the lower limb of the MOC [*Meinen et al*., 2012], and the western array was recently augmented with three additional CPIES instruments to improve estimation of the flows near that boundary. While the eastern boundary array was removed in December 2010, eight CPIES were deployed in September 2013 as part of a new array that will be completed in late 2013 involving both CPIES and tall moorings that will stretch as far offshore as the Walvis Ridge. Thanks to these existing and planned/future contributions, the developing South Atlantic MOC array will soon produce more complete, and accurate, measurements of the MOC at 34.5°S.

Appendix A: Transport Calculation Accuracy Estimate

[38] Assessment of the accuracy of a measurement is difficult when the methods involved include the use of a "residual" type term, because by its nature the residual will include all of the errors in the other terms. In terms of the MOC estimates for the 26.5°N array, the "residual" type calculation is the determination of the unknown barotropic contribution [*Kanzow et al*., 2007]. Based on the best assumptions possible, the accuracy of the daily transports at 26.5°N was determined to be about 3 Sv. At 34.5°S, the MOC has been estimated via a method that does not require a residual calculation (see text). As such, it is possible to determine a more explicit transport accuracy estimate involving fewer assumptions (see Table A1 for a brief overview).

[39] The accuracy of the 34.5°S MOC estimates made in this study was derived as follows: first, the accuracy of the geostrophic transports (both the relative to an assumed level of no motion and the reference velocity components) was determined; second, the Ekman transport accuracy was estimated by comparison to an independent wind product; and third, estimates of the unmeasured transport by flows on the shallow continental shelves and upper slopes were made using independent data sets and numerical models. In what follows, the accuracies of the various terms will be briefly explained, and the sources of error will be classified as either random sources of error or potential bias sources (see also Table A1).

Table A1. Estimates of Error Contributions to the MOC Accuracy (See Text)[a]

	Accuracy Estimate
Random Sources	
GEM look-up table accuracy	3.1 Sv
Scatter in τ_{PIES} versus τ_{1000} relationship	0.5 Sv
Measured τ accuracy	1.2 Sv
Baroclinic shear 1000–1500 dbar	2.3 Sv
Measured pressure accuracy	1.9 Sv
Ekman accuracy	1.4 Sv
West shelf missed variability	2.5 Sv
East shelf missed variability	2.5 Sv
Total random	5.9 Sv
Bias Sources	
Calibration of τ_{PIES} with concurrent CTDs	4.2 Sv
Accuracy of reference velocity time-mean	1.4 Sv
Ekman time-mean accuracy	0.02 Sv
Combined shelf missed time-mean	0.2 Sv
Total bias	4.4 Sv

[a]Totals are determined as the square root of the sum of the squares as appropriate.

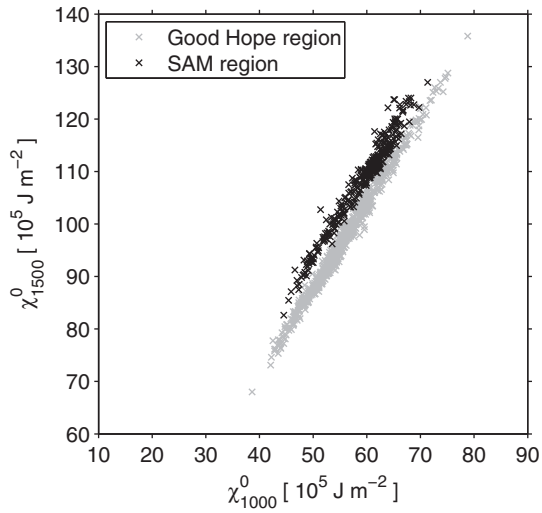

Figure A1. Relationship between the Fofonoff Potential (a.k.a. potential energy anomaly and/or baroclinic streamfunction) integrated between the surface and either 1000 dbar (x axis) or 1500 dbar (y axis). CTD data from Figure 2 are used—legend indicates symbol types for the data from the two regions.

[40] The random accuracy of the geostrophic velocity relative to an assumed level of no motion is perhaps the most complicated component as it is dependent on several sources of error:

[41] (1) The accuracy of the PIES measured travel time [0.5 ms; *Donohue et al*., 2010].

[42] (2) The scatter in the calibration relationship to convert the travel time at the PIES/CPIES actual depth into travel time on the fixed 1000 dbar level (0.2 ms, estimated as the root-mean-squared scatter in a linear fit between the simulated travel time at 1350 dbar versus the simulated travel time at 1000 dbar calculated from the available hydrographic data).

[43] (3) The accuracy of the GEM look-up tables (1.85×10^5 J m^{-2}, estimated as the root-mean-squared scatter in the relationship between simulated travel time at 1000 dbar and the baroclinic streamfunction, or Fofonoff Potential, at 1125 dbar—the approximate thickness of the MOC upper layer).

[44] (4) The scatter introduced by projecting the PIES/CPIES measured travel times (and their derived density and dynamic height profiles) downward using the GEM look-up tables from the instrument depths at ~1350 and 1000 dbar to the deepest observed transport-per-unit-depth sign change depths at ~1500 dbar for the transport integrations (1.4×10^5 J m^{-2}, estimated as the root-mean-squared scatter in a linear fit between the Fofonoff Potential at 1000 versus 1500 dbar—see Figure A1).

[45] The travel-time based accuracies were converted into transport using the slope of a linear fit between hydrography-simulated travel time at 1000 dbar and the Fofonoff Potential at 1125 dbar (-1.4×10^5 J m^{-2}/ms). Fofonoff Potential error bars were then converted into transport error bars with a constant density of 1030 kg m^{-3} and the local Coriolis parameter, under the assumption that the errors at Sites A and Z were independent of one another (i.e., their errors combine as the square-root of the sum of the squares).

[46] The other random sources of error in the MOC calculation are reference velocity variability accuracy, the Ekman variability accuracy, and the unobserved continental shelf variability. The sole random source of error in the determination of the reference velocity is the accuracy of the pressure gauges themselves (0.01 dbar after exponential-linear drift removal) [*Donohue et al*., 2010]. The Ekman transport random accuracy was estimated as the standard deviation of the difference between the Ekman transport integrated between Sites A and Z along 34.5°S using either the CCMP wind product described in the text or the NCEP/NCAR reanalysis winds (downloaded from ftp://ftp.cdc.noaa.gov/pub/Datasets/ncep.reanalysis/surface_gauss/) using the same drag coefficient and air density discussed in the text. Note that the NCEP/NCAR winds and the CCMP winds are not completely independent, as both incorporate many of the same observations, however the assumption here is that the largest source of error in the wind products is based on the gridding and interpolation techniques applied, and those are different for these two products. The resulting standard deviation between the two Ekman transport time series during the 2009–2010 time period was 1.4 Sv. The random errors associated with the unobserved continental upper slopes and shelves inshore of Sites A and Z were determined by evaluating the standard deviation of the transport in the two inshore domains from three data sets: the 27 year OFES model run described in the text (1.6 Sv and 2.2 Sv for the west and east shelves, respectively); the ~6 year NEMO model run described in the text (3.3 Sv and 4.7 Sv, respectively); and a data set of ~18 XBT sections from those described by *Garzoli et al*. [2013] that most closely approximated the latitude of the pilot arrays (2.5 Sv and 0.8 Sv, respectively). The average of these values (2.5 Sv) was used as the random "error bar" associated with the transport on each shelf. The various random sources of error were all assumed to be independent of one another and were combined in a square-root of the sum of squares manner to yield an overall random accuracy for the daily MOC values of 5.9 Sv.

[47] Not all potential sources of error in the MOC calculation can be considered random—several would apply to the resulting time-mean MOC (and would have no impact on the time variations). These sources are as follows:

[48] (1) The calibration of the PIES/CPIES measured travel times into travel time at 1000 dbar using concurrent CTD profiles. The time-varying baroclinic structure between 1000 dbar and the actual depth of the PIES/CPIES has already been accounted for in one of the random error sources, however when applying the calibration CTD data to the PIES/CPIES measured travel times it is possible that the time-mean of the resulting calibrated travel time record could be off, and this would result in an artificial time-mean density gradient between Sites A and Z, and hence a transport error for the estimated MOC. This potential error source was estimated by calculating the root-mean-squared difference between simulated travel time measurements from colocated CTD casts at three of the western array sites and the coincident calibrated PIES/CPIES travel time values (1.8 ms). This error estimate was converted to a transport error bar in the same manner as the random travel time errors, yielding 4.2 Sv.

[49] (2) The application of the absolute reference velocity includes a time-mean derived from other sources as discussed in the text. The accuracy of the applied time-mean reference velocity was estimated as the difference between the three sources: the 27 year OFES run described herein (-0.0007 m s^{-1}); the ~7 year NEMO run described herein (-0.0009 m s^{-1}); and a gridded Argo and satellite altimetry climatological velocity product (-0.0004 m s^{-1}) (C. Schmid, personal communication, 2013). The differences between these estimates are roughly equal to about 0.0002 m s^{-1}, which is translated into transport using a mean basin width of 6.3×10^6 m and a mean upper cell thickness of about 1125 m; the resulting transport error is 1.4 Sv.

[50] (3) The time-mean Ekman accuracy is determined simply as the time-mean difference in Ekman transports calculated using the CCMP and NCEP/NCAR wind products along 34.5°S between Sites A and Z using the same constant drag coefficient and air density discussed in the text over the time period 2009–2010. The resulting mean difference is very small, only 0.02 Sv.

[51] (4) The potential bias associated with the unobserved upper slopes and shallow shelves inshore of Sites A and Z was estimated using the same three products (OFES, NEMO, XBT sections) as the associated random error. The mean shelf transports (combining west and east shelves) for the three models/data sets are -0.8 Sv, -0.5 Sv, and -0.9 Sv, respectively. The average of these values is -0.7 Sv, and the difference of the individual sources from the mean is approximately 0.2 Sv, which is used as the error bar for this source.

[52] These potential bias sources of error are independent of one another (e.g., could be of differing sign), so the total estimated bias error was determined as the square-root of the sum of the squares of these bias sources, yielding 4.4 Sv as the potential bias error.

[53] **Acknowledgments.** The authors would like to express their great appreciation to the crews and officers of the research vessels which have supported this program to date, including the Brazilian research vessels N.H. Cruzeiro do Sul and N. Oc. Alpha-Crucis, the Argentine research vessel A.R.A. Puerto Deseado (CONICET), the French research vessel Marion Dufresne II (IPEV), the South African research vessel Agulhas, and the Russian research vessel Akademik Vavilov. Also our sincere thanks to the scientific participants who have collected the PIES/CPIES data during the cruises: Rigoberto Garcia, Ulises Rivero, Pedro Peña, Aldo Firpo, Norbert Cortes, Thierry Terre, and Stephan Leizour. And our thanks to those who have helped coordinate these challenging international cruise collaborations, especially Ariel Troisi and Raul Guerrero in Argentina, Luiz Nonnato, Carlos França and Francisco Vicentini in Brazil, and Isabelle Ansorge and Sebastiaan Swart in South Africa. Claudia Schmid kindly provided the Argo/Altimeter time-mean reference velocity and Qi Yao calculated the shelf transports from XBT. Many thanks also to the generous researchers who provided us with the OFES model output, especially Yoshikazu Sasai at JAMSTEC, and Ricardo Matano at OSU. Bruno Blanke at LPO and Yann Drillet at MERCATOR kindly provided the

ORCA12/NEMO output as well as several helpful suggestions on improving an earlier draft of this paper. Rick Lumpkin, Libby Johns, and three anonymous reviewers also provided helpful suggestions for improving this manuscript, and their help is gratefully acknowledged. S.S. acknowledges the support of grants from the Institut National des Sciences de l'Univers (INSU), the IFREMER programme "Circulation Océanique," the French Polar Institut Paul-Emile Victor (IPEV), and the Agence Nationale de la Recherche (ANR). A.R.P. and E.J.D.C. acknowledge the support of grant CRN3070 from the Inter-American Institute for Global Change Research, which is supported by the US National Science Foundation (GEO-1128040). E.J.D.C. also acknowledges the support of the São Paulo Research Foundation (FAPESP—Processes 2011/50552-4 and 2010/06147-5). R.C.P., S.D., and S.L.G.'s work on this study was carried out in part under the auspices of the Cooperative Institute for Marine and Atmospheric Studies (CIMAS), a Cooperative Institute of the University of Miami and the National Oceanic and Atmospheric Administration (NOAA), cooperative agreement NA10OAR4320143. C.S.M., R.C.P., S.D., S.L.G., and M.O.B. also acknowledge support from the NOAA Atlantic Oceanographic and Meteorological Laboratory and the NOAA Climate Program Office.

References

Atlas, R., R. N. Hoffman, J. Ardizzone, S. M. Leidner, J. C. Jusem, D. K. Smith, and D. Gombos (2011), A cross-calibrated, multiplatform ocean surface wind velocity product for meteorological and oceanographic applications, *Bull. Am. Meteorol. Soc.*, *92*, 157–174, doi:10.1175/2010BAMS2946.1.

Baringer, M. O., and S. L. Garzoli (2007), Meridional heat transport determined with expendable bathythermographs. Part I: Error estimates from model and hydrographic data, *Deep Sea Res., Part I*, *54*(8), 1390–1401.

Barnier, B., et al. (2006), Impact of partial steps and momentum advection schemes in a global circulation model at eddy permitting resolution, *Ocean Dyn.*, *56*(5–6), 543–567, doi:10.1007/s10236-006-0082-1.

Bryden, H. L., H. R. Longworth, and S. A. Cunningham (2005), Slowing of the Atlantic meridional overturning circulation at 25°N, *Nature*, *438*, 655–657.

Bryden, H. L., B. A. King, and G. D. McCarthy (2011), South Atlantic overturning circulation at 24°S, *J. Mar. Res.*, *69*(1), 38–55.

Chereskin, T. K., K. A. Donohue, D. R. Watts, K. L. Tracey, Y. L. Firing, and A. L. Cutting (2009), Strong bottom currents and cyclogenesis in Drake Passage, *Geophys. Res. Lett.*, *36*, L23602, doi:10.1029/2009GL040940.

Chidichimo, M. P., T. Kanzow, S. A. Cunningham, W. E. Johns, and J. Marotzke (2010), The contribution of eastern-boundary density variations to the Atlantic meridional overturning circulation at 26.5° N, *Ocean Sci.*, *6*, 475–490, doi:10.5194/os-6-475-2010.

Cunningham, S. A., et al. (2007), Temporal variability of the Atlantic meridional overturning circulation at 26.5°N, *Science*, *317*, 935, doi:10.1126/science.1141304.

Dee, D. P., et al. (2011), The ERA-Interim reanalysis: Configuration and performance of the data assimilation system, *Q. J. R. Meteorol. Soc.*, *137*, 553–597, doi:10.1002/qj.828.

Del Grosso, V. A. (1974), New equation for the speed of sound in natural waters (with comparisons to other equations), *J. Acoust. Soc. Am.*, *56*, 1084–1091.

Dijkstra, H. A. (2007), Characterization of the multiple equilibria regime in a global ocean model, *Tellus, Ser. A*, *59*, 695–705.

Dong, S., S. L. Garzoli, M. O. Baringer, C. S. Meinen, and G. J. Goni (2009), Interannual variations in the Atlantic meridional overturning circulation and its relationship with the net northward heat transport in the South Atlantic, *Geophys. Res. Lett.*, *36*, L20606, doi:10.1029/2009GL039356.

Dong, S., S. L. Garzoli, and M. O. Baringer (2011), The role of inter-ocean exchanges on decadal variations of the northward heat transport in the South Atlantic, *J. Phys. Oceanogr.*, *41*, 1498–1511.

Donohue, K. D., D. R. Watts, K. L. Tracey, A. D. Greene, and M. Kennelly (2010), Mapping circulation in the Kuroshio extension with an array of current and pressure recording inverted echo sounders, *J. Atmos. Oceanic Technol.*, *27*, 507–527, doi:10.1175/2009JTECHO686.1.

Drijfhout, S. S., S. L. Weber, and E. van der Swaluw (2011), The stability of the MOC as diagnosed from model projections for pre-industrial, present and future climates, *Clim. Dyn.*, *37*, 1575–1586, doi:10.1007/s00382-0-10-0930-z.

Emery, W. J., and R. E. Thomson (1997), *Data Analysis Methods in Physical Oceanography*, Pergamon, Oxford, U. K.

Fofonoff, N. P. (1962), Dynamics of ocean currents, in *The Sea: Ideas and Observations on Progress in the Study of the Seas*, vol. *1*, edited by M. N. Hill, chap. 3, pp. 323–396, Wiley-Interscience, New York.

Fu, L.-L. (1981), The general circulation and meridional heat transport of the subtropical South Atlantic determined by inverse methods, *J. Phys. Oceanogr.*, *11*, 1171–1193.

Garzoli, S. L. (1993), Geostrophic velocity and transport variability in the Brazil-Malvinas Confluence, *Deep Sea Res., Part I*, *40*(7), 1379–1403.

Garzoli, S. L., and M. O. Baringer (2007), Meridional heat transport determined with expendable bathythermographs. Part II: South Atlantic transport, *Deep Sea Res., Part I*, *54*(8), 1402–1420.

Garzoli, S. L., and A. L. Gordon (1996), Origins and variability of the Benguela Current, *J. Geophys. Res.*, *101*(C1), 897–906.

Garzoli, S. L., and R. P. Matano (2011), The South Atlantic and the Atlantic meridional overturning circulation, *Deep Sea Res., Part II*, *58*(17–18), 1837–1847.

Garzoli, S. L., M. O. Baringer, S. Dong, R. C. Perez, and Q. Yao (2013), South Atlantic meridional fluxes, *Deep Sea Res., Part I*, *71*, 21–32, doi:10.1016/j.dsr.2012.09.003.

Jochumsen, K., D. Quadfasel, H. Valdimarsson, and S. Jónsson (2012), Variability of the Denmark Strait overflow: Moored time series from 1996–2011, *J. Geophys. Res.*, *117*, C12003, doi:10.1029/2012JC008244.

Johns, W. E., et al. (2011), Continuous array-based estimates of Atlantic Ocean heat transport at 26.5°N, *J. Clim.*, *24*(10), 2429–2449.

Kanzow, T., S. A. Cunningham, D. Rayner, J. J.-M. Hirshi, W. E. Johns, M. O. Baringer, H. L. Bryden, L. M. Beal, C. S. Meinen, and J. Marotzke (2007), Observed flow compensation associated with the meridional overturning at 26.5°N in the Atlantic, *Science*, *317*, 938, doi:10.1126/science.1141293.

Kanzow, T., U. Send, and M. McCartney (2008), On the variability of the deep meridional transports in the tropical North Atlantic, *Deep Sea Res., Part I*, *55*(12), 1601–1623, doi:10.1016/j.dsr.2008.07.011.

Kanzow, T., H. L. Johnson, D. P. Marshall, S. A. Cunningham, J. J.-M. Hirschi, A. Mujahid, H. L. Bryden, and W. E. Johns (2009), Basinwide integrated volume transports in an eddy-filled ocean, *J. Phys. Oceanogr.*, *39*, 3091–3110, doi:10.1175/2009JPO4185.1.

Kanzow, T., et al. (2010), Seasonal variability of the Atlantic meridional overturning circulation at 26.5°N, *J. Clim.*, *23*, 5678–5698, doi:10.1175/2010JCLI3389.1.

Large, W. G., and S. G. Yeager (2009), The global climatology of an interannually varying air-sea flux data set, *Clim. Dyn.*, *33*, 341–364, doi:10.1007/s00382-008-0441-3.

Levitus, S., J. Antonov, and T. Boyer (2005), Warming of the world ocean, 1955–2003, *Geophys. Res. Lett.*, *32*, L02604, doi:10.1029/2004GL021592.

Madec, G. (2008), NEMO reference manual, ocean dynamics component: NEMO-OPA. Preliminary version, Tech. Rep. 27, Note du Pôle de modélisation, Inst. Pierre-Simon Laplace, Paris, France, ISSN 1288–1619.

Masumoto, Y., et al. (2004), A fifty-year Eddy resolving simulation of the world ocean—Preliminary outcomes of OFES (OGCM for the Earth simulator), *J. Earth Simulator*, *1*, 3556.

McCarthy, G., E. McDonagh, and B. King (2011), Decadal variability of thermocline and intermediate Waters at 24°S in the South Atlantic, *J. Phys. Oceanogr.*, *41*, 157–165, doi:10.1175/2010JPO4467.1.

McCarthy, G. D., E. Frajka-Williams, W. Johns, M. Baringer, C. Meinen, H. Bryden, D. Rayner, A. Duchez, C. Roberts, and S. Cunningham (2012), Observed interannual variability of the Atlantic meridional overturning circulation at 26.5°N, *Geophys. Res. Lett.*, *39*, L19609, doi:10.1029/2012GL052933.

McDonagh, E. L., and B. A. King (2005), Oceanic fluxes in the South Atlantic, *J. Phys. Oceanogr.*, *35*, 109–122, doi:10.1175/JPO-2666.1.

Meinen, C. S. (2001), Structure of the North Atlantic Current in stream-coordinates and the circulation in the Newfoundland Basin, *Deep Sea Res., Part I*, *48*(7), 1553–1580.

Meinen, C. S., and D. R. Watts (2000), Vertical structure and transport on a transect across the North Atlantic Current near 42°N: Time series and mean, *J. Geophys. Res.*, *105*(C9), 21,869–21,891.

Meinen, C. S., S. L. Garzoli, W. E. Johns, and M. O. Baringer (2004), Transport variability of the deep western boundary current and the Antilles current off Abaco Island, Bahamas, *Deep Sea Res., Part I*, *51*(11), 1397–1415.

Meinen, C. S., A. R. Piola, R. C. Perez, and S. L. Garzoli (2012), Deep western boundary current transport variability in the South Atlantic: Preliminary results from a pilot array at 34.5°S, *Ocean Sci.*, *8*, 1041–1054, doi:10.5194/os-8–1041-2012.

Meinen, C. S., W. E. Johns, S. L. Garzoli, E. van Sebille, D. Rayner, T. Kanzow, and M. O. Baringer (2013), Variability of the deep western boundary current at 26.5°N during 2004–2009, *Deep Sea Res., Part II*, *85*, 154–168, doi:10.1016/j.dsr2.2012.07.036.

Palma, E. D., R. P. Matano, and A. R. Piola (2008), A numerical study of the southwestern Atlantic shelf circulation, *J. Geophys. Res.*, *113*, C11010, doi:10.1029/2007JC004720.

Peña-Molino, B., T. M. Joyce, and J. M. Toole (2012), Variability in the deep western boundary current: Local versus remote forcing, *J. Geophys. Res.*, *117*, C12022, doi:10.1029/2012JC008369.

Perez, R. C., S. L. Garzoli, C. S. Meinen, and R. P. Matano (2011), Geostrophic velocity measurement techniques for the meridional overturning circulation and meridional heat transport in the South Atlantic, *J. Atmos. Oceanic Technol.*, *28*, 1504–1521, doi:10.1175/JTECH-D-11-00058.1.

Rayner, D., et al. (2011), Monitoring the Atlantic meridional overturning circulation, *Deep Sea Res., Part I*, *48*, 1744–1753, doi:10.1016/j.dsr2.2010.10.056.

Rossby, T. (1969), On monitoring depth variations of the main thermocline acoustically, *J. Geophys. Res.*, *74*(23), 5542–5546.

Sasaki, H., M. Nonaka, Y. Sasai, H. Uehara, and H. Sakuma (2008), An eddy-resolving hindcast simulation of the quasiglobal ocean from 1950 to 2003 on the Earth simulator, in *High Resolution Numerical Modelling of the Atmosphere and Ocean*, edited by K. Hamilton and W. Ohfuchi, pp. 157–185, Springer, New York.

Saunders, P. M., and B. A. King (1995), Oceanic fluxes on the WOCE A11 section, *J. Phys. Oceanogr.*, *25*, 1942–1958.

Send, U., M. Lankhorst, and T. Kanzow (2011), Observation of decadal change in the Atlantic meridional overturning circulation using 10 years of continuous transport data, *Geophys. Res. Lett.*, *38*, L24606, doi:10.1029/2011GL049801.

Smith, W. H. F., and D. T. Sandwell (1997), Global Sea floor topography from satellite altimetry and ship depth soundings, *Science 277 (5334)*, 1956–1962.

Speich, S., and F. Dehairs (2008), The MD166 BONUS-GOODHOPE Cruise, LPO UMR 6523 CNRS-IFREMERIRD-UBO technical report—IPEV technical, 245 pp. + Annexes, The University of Brest (UBO), Brest, France.

Stouffer, R. J., J. Yin, and J. M. Gregory (2006), Investigating the causes of the response of the thermohaline circulation to past and future climate changes, *J. Clim.*, *19*(8), 1365–1387.

Thompson, R. O. R. Y. (1979), Coherence significance levels, *J. Atmos. Sci.*, *36*(10), 2020–2021.

Toole, J. M., R. G. Curry, T. M. Joyce, M. McCartney, and B. Peña-Molino (2011), Transport of the North Atlantic deep western boundary current at about 39°N, 70°W: 2004–2008, *Deep Sea Res., Part II*, *58*, 1768–1780.

Vellinga, M., and R. A. Wood (2002), Global climatic impacts of a collapse of the Atlantic thermohaline circulation, *Clim. Change*, *54*(3), 251–267.

Watts, D. R., and H. Kontoyiannis (1990), Deep-ocean bottom pressure measurement: Drift removal and performance, *J. Atmos. Oceanic Technol.*, *7*(2), 296–306.

Watts, D. R., and H. T. Rossby (1977), Measuring dynamic heights with Inverted Echo Sounders: Results from MODE, *J. Phys. Oceanogr.*, *7*, 345–358.

Watts, D. R., K. L. Tracey, J. M. Bane, and T. J. Shay (1995), Gulf Stream path and thermocline structure near 74°W and 68°W, *J. Geophys. Res.*, *100*(C9), 18,291–18,312.

Watts, D. R., C. Sun, and S. Rintoul (2001), A two-dimensional gravest empirical mode determined from hydrographic observations in the Subantarctic Front, *J. Phys. Oceanogr.*, *31*(8), 2186–2209.

Weisberg, R. H., and C. Wang (1997), Slow variability in the equatorial west-central Pacific in relation to ENSO, *J. Clim.*, *10*, 1998–2017.

Willis, J. K. (2010), Can in situ floats and satellite altimeters detect long-term changes in Atlantic Ocean overturning?, *Geophys. Res. Lett.*, *37*, L06602, doi:10.1029/2010GL042372.

Willis, J. K., and L.-L. Fu (2008), Combining altimeter and subsurface float data to estimate the time-averaged circulation in the upper ocean, *J. Geophys. Res.*, *113*, C12017, doi:10.1029/2007JC004690.

Zhang, D., R. Msadek, M. J. McPhaden, and T. Delworth (2011), Multidecadal variability of the North Brazil current and its connection to the Atlantic meridional overturning circulation, *J. Geophys. Res.*, *116*, C04012, doi:10.1029/2010JC006812.

Zhang, R. (2010), Latitudinal dependence of Atlantic meridional overturning circulation (AMOC) variations, *Geophys. Res. Lett.*, *37*, L16703, doi:10.1029/2010GL044474.

Zhang, R., and T. L. Delworth (2006), Impact of Atlantic multidecadal oscillations on India/Sahel rainfall and Atlantic hurricanes, *Geophys. Res. Lett.*, *33*, L17712, doi:10.1029/2006GL026267.